

Detection of standing internal gravity waves in experiments with convection over a wavy heated wall

L. Barel, A. Eidelman, T. Elperin, G. Fleurov, N. Kleeorin, A. Levy, I. Rogachevskii,* and O. Shildkrot
*The Pearlstone Center for Aeronautical Engineering Studies, Department of Mechanical Engineering,
 Ben-Gurion University of the Negev, P.O.Box 653, Beer-Sheva 84105, Israel*

(Dated: June 2, 2020)

Convection over a wavy heated bottom wall in the air flow has been studied in experiments with the Rayleigh number $\sim 10^8$. It is shown that the mean temperature gradient in the flow core inside a large-scale circulation is directed upward, that corresponds to the stably stratified flow. In the experiments with a wavy heated bottom wall, we detect large-scale standing internal gravity waves excited in the regions with the stably stratified flow. The wavelength and the period of these waves are much larger than the turbulent spatial and time scales, respectively. In particular, the frequencies of the observed large-scale waves vary from 0.01 Hz to 0.1 Hz, while the turbulent time in the integral scale is about 0.5 s. The measured spectrum of these waves contains several localized maxima, that implies an existence of waveguide resonators for the internal gravity waves. On the other hand, in experiments with a smooth plane bottom wall performed at the same mean temperature difference between bottom and upper walls, there are less locations with a stably stratified flow, and the internal gravity waves are not observed.

I. INTRODUCTION

Temperature stratified turbulence in convective and stably stratified flows has been investigated theoretically, experimentally and in numerical simulations due to numerous applications in geophysical, astrophysical and industrial flows. [1–10] One of the key ingredients of stably stratified flows are internal gravity waves. In atmospheric and oceanic turbulence they have been a subject of intense research. [11–31] In the atmosphere, internal gravity waves exist at scales ranging from meters to kilometers, and are measured by direct probing or remote sensing using radars and lidars. [17, 25] The sources of internal gravity waves can be flows over complex terrain, strong wind shears, convective and other local-scale motions underlying the stably stratified layer, and wave-wave interactions. [17, 18] The internal gravity waves propagation is complicated by variable wind and density profiles causing refraction, reflection, focusing, and ducting.

The internal gravity waves can strongly affect the small-scale turbulence. In particular, these waves create additional productions of turbulent energy and additional vertical turbulent fluxes of momentum and heat. In particular, the waves emitted at a certain level, propagate upward, and the losses of wave energy cause the production of turbulence energy. These effects have been studied theoretically, where the energy- and flux-budget (EFB) turbulence closure theory which accounts for large-scale internal gravity waves (IGW) for stably stratified atmospheric flows has been developed. [32, 33] For the stationary (in statistical sense) and homogeneous turbulence, the EFB theory without large-scale IGW yields universal dependencies of the main turbulence parameters on the flux Richardson number (defined

as the ratio of the consumption of turbulent kinetic energy (TKE) needed for overtaking buoyancy forces to the TKE production by the velocity shear). [34–37] Due to the large-scale IGW, these dependencies lose their universality. [32, 33] The maximum value of the flux Richardson number (universal constant ≈ 0.25 in the absence of the large-scale IGW) becomes strongly variable. In the vertically homogeneous stratification, the flux Richardson number increases with increasing wave energy and can even exceed 1. For heterogeneous stratification, when internal gravity waves propagate towards stronger stratification, the maximal flux Richardson number decreases with increasing wave energy and even can reach very small values. [32, 33]

Internal gravity waves also reduce the anisotropy of turbulence: in contrast to the mean wind shear, which generates only horizontal TKE, internal gravity waves generate both horizontal and vertical TKE. A well-known effect of internal gravity waves is their direct contribution to the vertical transport of momentum. Depending on the direction of the wave propagation (downward or upward), the internal gravity waves either strengthen or weaken the total vertical flux of momentum. [32, 33]

Even in a convective turbulence, stably stratified regions can be formed, where the mean temperature gradient in the flow core inside the large-scale circulation is directed upward. [38, 39] In these regions internal gravity waves are generated, which affect the turbulence. In spite of many studies of stratified turbulence and internal gravity waves, a mechanism of formation of the stably stratified regions in convective turbulence, and generation of internal gravity waves in these regions is not comprehensively studied and understood.

In various flows a complex terrain (i.e., canopy and various topography) strongly affects the stratified turbulence. [40] It changes local temperature gradients, heat and mass fluxes, and affects a local structure of fluid flows. Therefore, one of the important questions — what

* gary@bgu.ac.il

is the effect of complex terrain on convective and stably stratified turbulence?

To model the effect of complex terrain, the Rayleigh-Bénard convection (RBC) with modulated boundaries has been investigated. [38, 41–47] In particular, the influence of a modulated boundary on RBC by a lithographically fabricated periodic texture on the bottom plate has been studied experimentally. [44] The different convection patterns have been obtained by varying the Rayleigh number and the wave number of the modulated boundary. For small Rayleigh numbers, convection takes the form of straight parallel rolls. With increasing Rayleigh number, a secondary instability is excited and the convection has more complex patterns. [44] This secondary instability has been studied theoretically and numerically. [45]

The roughness effect on the heat transport in RBC has been investigated in two-dimensional numerical simulations by varying the height and wavelength of the roughness elements where the sinusoidal roughness profile has been chosen. [38, 46] The ultimate regime of thermal convection (when the boundary layers undergo a transition leading to the generation of smaller scales near the boundaries that increase the systems efficiency in transporting the heat) has been found in [38]. This regime in which the heat flux becomes independent of the molecular properties of the fluid, has been predicted. [49, 50] The first experiment designed to use roughness to reach the ultimate regime at accessible Rayleigh numbers has been made. [47] One of the key role of the roughness elements is the production and release of the plumes from the roughness elements, resulting formation of larger plumes. This can cause an increase in the efficiency of the heat transfer. [38, 48] The existence of two universal regimes in RBC, namely the ultimate regime and the classical boundary-layer-controlled regime with increased Rayleigh number, have been demonstrated. [46] The transition from the first to the second regime is determined by the competition between bulk and boundary layer flow. The bulk-dominated regime corresponds to the ultimate regime.

In the present study, we investigate another aspects related to the roughness effect on turbulent convection. In particular, we study formation of the stably stratified regions and excitation of internal gravity waves in laboratory experiments with turbulent convection over a wavy heated bottom wall in the air as the working fluid. An interactions of the large-scale convective circulation with the wavy heated bottom wall strongly modifies the mean temperature spatial distribution. In particular, stably stratified regions in the flow core are formed and large-scale standing internal gravity waves are excited. The measured spectrum of the waves contains several localized maxima, that indicates an existence of the waveguide resonators of the internal gravity waves in the stably stratified flow regions. We have compared results of these experiments to those obtained in experiments with a smooth plane bottom wall at the same temperature

difference between bottom and upper walls.

This paper is organized as follows. In Section II we present theoretical analysis which allows us to determine the frequencies of the standing internal gravity waves in stably stratified flow. In Section III we describe the experimental set-up and instrumentation for laboratory study of the internal gravity waves. The results of the laboratory experiments are discussed in Section IV. Finally, conclusions are drawn in Section V.

II. INTERNAL GRAVITY WAVES

Let us first consider the internal gravity waves in a stably stratified fluid flow in the absence of turbulence and neglecting dissipations. These waves are described by the linearized momentum and entropy equations written in the Boussinesq approximation [1, 13–15]

$$\frac{\partial \mathbf{V}^W}{\partial t} = -\frac{\nabla P^W}{\rho_{\text{eq}}} + g S^W \mathbf{e}, \quad (1)$$

$$\frac{\partial S^W}{\partial t} = -g^{-1} N^2 \mathbf{V}^W \cdot \mathbf{e}, \quad (2)$$

where

$$S^W = c_v \left[(1 - \gamma) \frac{P^W}{P_{\text{eq}}} + \gamma \frac{T^W}{T_{\text{eq}}} \right], \quad (3)$$

the wave fields \mathbf{V}^W , P^W , S^W and T^W are the perturbations of the velocity, pressure, entropy and temperature, respectively, \mathbf{e} is the vertical unit vector, \mathbf{g} is the acceleration due to gravity, and $\gamma = c_p/c_v$ is the ratio of the specific heats, c_p and c_v are the specific heats at constant pressure and volume, respectively. The Brunt-Väisälä frequency is $N(z) = (g \nabla_z S_{\text{eq}})^{1/2}$, where

$$\nabla_z S_{\text{eq}} = c_v [(1 - \gamma) \nabla_z \ln P_{\text{eq}} + \gamma \nabla_z \ln T_{\text{eq}}], \quad (4)$$

and the fields S_{eq} , P_{eq} , T_{eq} and ρ_{eq} are the entropy, pressure temperature and density at an equilibrium given by the following equations: $\mathbf{V}_{\text{eq}} = 0$ and $\nabla P_{\text{eq}} = \rho_{\text{eq}} \mathbf{g}$, where $\mathbf{V}_{\text{eq}}0$ is the velocity at an equilibrium. For conditions pertinent to the laboratory experiments discussed in the next sections, $\nabla P_{\text{eq}} \approx 0$, so that $\nabla_z S_{\text{eq}} \approx c_p \nabla_z \ln T_{\text{eq}}$. The classical Boussinesq approximation with $\text{div } \mathbf{V}^W = 0$ is applied here.

Equations (1) and (2) yield the frequency ω of the internal gravity waves:

$$\omega = N(z) \frac{k_h}{k}, \quad (5)$$

where $\mathbf{k} = \mathbf{k}_h + \mathbf{e}k_z$ is the wave vector and $\mathbf{k}_h = (k_x, k_y)$ is the wave vector in the horizontal direction. Propagation of the internal gravity waves in the stably stratified flow in the approximation of geometrical optics is determined by the following Hamiltonian equations:

$$\frac{\partial \mathbf{r}}{\partial t} = \frac{\partial \omega}{\partial \mathbf{k}}, \quad (6)$$

$$\frac{\partial \mathbf{k}}{\partial t} = -\frac{\partial \omega}{\partial \mathbf{r}}, \quad (7)$$

where \mathbf{r} is the radius-vector of the centre of the wave packet. [51]) Since the Brunt-Väisälä frequency $N = N(z)$, the only non-zero spatial derivative, $\nabla_z \omega \neq 0$, is in the vertical direction. Therefore, Eq. (7) yields $\mathbf{k}_h = \text{const}$. The vertical component of the wave vector $k_z = k_z(z)$ is determined from Eq. (5):

$$k_z(z) = k_h \left(\frac{N^2(z)}{\omega^2} - 1 \right)^{1/2}. \quad (8)$$

We perform standard calculations by taking twice **curl** to exclude the pressure term in Eq. (1), calculating the time derivative of the obtained equation and using Eq. (2). This procedure yields the following equation:

$$\frac{\partial^2}{\partial t^2} \Delta \mathbf{V}^W = [\nabla(\mathbf{e} \cdot \nabla) - \mathbf{e}\Delta] V_z^W N^2(z), \quad (9)$$

which is equivalent to the system of equations for the vertical and horizontal velocity components:

$$\frac{\partial^2}{\partial t^2} \Delta V_z^W = -N^2(z) \Delta_{\perp} V_z^W, \quad (10)$$

$$\frac{\partial^2}{\partial t^2} \Delta \mathbf{V}_{\perp}^W = \nabla_{\perp} \nabla_z^2 [V_z^W N^2(z)]. \quad (11)$$

Here $\mathbf{V}^W = \mathbf{V}_{\perp}^W + \mathbf{e}V_z^W$ with $\mathbf{V}_{\perp}^W = (V_x^W, V_y^W)$ being the horizontal velocity and $\Delta = \Delta_{\perp} + \nabla_z^2$. Solution of Eq. (10) for the vertical velocity $V_z^W(t, \mathbf{r})$ we seek for in the form of standing internal gravity waves existing in the range $z_{\min} \leq z \leq z_{\max}$:

$$V_z^W(t, \mathbf{r}) = V_* \cos(\omega t) \cos(\mathbf{k}_h \cdot \mathbf{r}) \times \sin \left(\int_{z_{\min}}^z k_z(z') dz' + \varphi \right), \quad (12)$$

where V_* is the amplitude of the vertical velocity for the wave field. Substituting Eq. (12) into Eq. (11), we determine perturbations of the horizontal velocity $\mathbf{V}_{\perp}^W(t, \mathbf{r})$ for the wave field as

$$\mathbf{V}_{\perp}^W(t, \mathbf{r}) = -\mathbf{k}_h \frac{k_z(z)}{k_h^2} V_* \cos(\omega t) \sin(\mathbf{k}_h \cdot \mathbf{r}) \times \cos \left(\int_{z_{\min}}^z k_z(z') dz' + \varphi \right). \quad (13)$$

Using Eqs. (2) and (12), we obtain solution for perturbations of the entropy $S^W(t, \mathbf{r})$:

$$S^W(t, \mathbf{r}) = \frac{N^2(z)}{g\omega} V_* \sin(\omega t) \cos(\mathbf{k}_h \cdot \mathbf{r}) \times \sin \left(\int_{z_{\min}}^z k_z(z') dz' + \varphi \right). \quad (14)$$

The solution (12) should satisfy the following boundary conditions: $V_z^W(z = z_{\min}) = 0$ and $V_z^W(z \approx z_{\max}) = 0$. The latter boundary condition at the vicinity of $z \approx z_{\max}$ implies that

$$\int_{z_{\min}}^{z_{\max}} k_z(z') dz' = \pi \left(m + \frac{1}{4} \right), \quad (15)$$

where z_{\max} is the reflection (or "turning") point in which $k_z(z = z_{\max}) = 0$. To get the condition (15), we use an analogy with the behavior of the wave function near the turning points in the semi-classical limit applied in quantum mechanics. [52, 53] The wave functions are described in terms of the Airy functions, and Eq. (15) is analogous to the Bohr-Sommerfeld quantization condition. In particular, the phase φ in Eqs. (12)–(14) is determined using asymptotic solution of Eq. (10) in the vicinity of the turning points:

$$V_z^W = \frac{1}{2} \xi^{-1/4} \exp \left(-\frac{2}{3} \xi^{3/2} \right), \quad \text{for } \xi \gg 1,$$

$$V_z^W = \frac{1}{2} |\xi|^{-1/4} \sin \left(\frac{2}{3} |\xi|^{3/2} + \frac{\pi}{4} \right), \quad \text{for } |\xi| \ll 1, \quad (16)$$

where $\xi \propto z_{\max} - z$. Equation (15) allows us to determine the frequencies of the standing internal gravity waves for the quadratic profile of the Brunt-Väisälä frequency $N^2(z) = N_0^2(1 - z^2/L_N^2)$. In particular, calculating the integral $\int_{z_{\min}}^{z_{\max}} k_z(z') dz'$, we obtain:

$$\omega_m = \frac{N_0}{k_h L_N} \left\{ \left[\left(m + \frac{1}{4} \right)^2 + (k_h L_N)^2 \right]^{1/2} - \left(m + \frac{1}{4} \right) \right\}, \quad (17)$$

where L_N is the characteristic scale of the Brunt-Väisälä frequency variations, and $m = 0, 1, 2, \dots$. Equation (17) implies the existence of a discrete spectrum of the standing internal gravity waves. In the long wavelength limit, $k_h L_N \ll 1$, Eq. (17) yields

$$\omega_m = \frac{2N_0}{4m+1} k_h L_N. \quad (18)$$

We will apply Eq. (17) in the experimental study of convection over a wavy heated bottom surface, where the large-scale internal gravity waves are excited in the stably stratified regions formed inside the flow core of the large-scale circulation.

III. EXPERIMENTAL SET-UP

In this section we describe the experimental set-up. The experiments have been conducted in air as the working fluid in rectangular chamber with dimensions $L_x \times L_y \times L_z$, where $L_x = L_z = 26$ cm, $L_y = 56$ cm and the axis z is in the vertical direction. The side walls of the chamber are made of transparent Perspex with the thickness of 1 cm.

A vertical mean temperature gradient in the turbulent air flow is formed by attaching two aluminium heat exchangers to the bottom and top walls of the test section (a heated bottom and a cooled top wall of the chamber). The top plate is a bottom wall of the tank with cooling water. Cold water is pumped into the cooling system

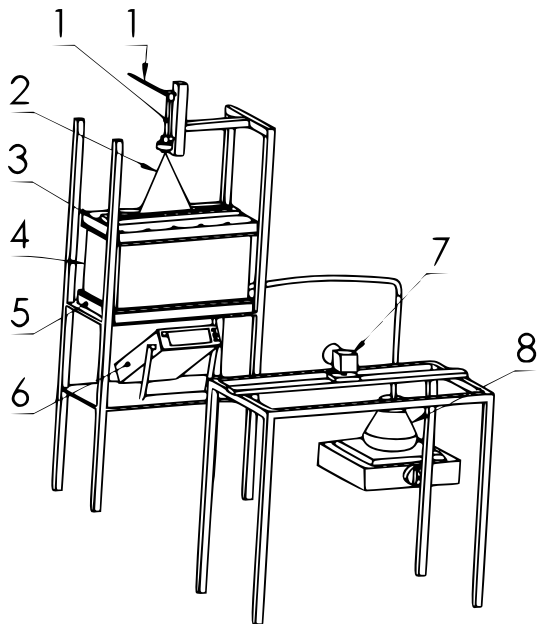


FIG. 1. A sketch of the experimental set-up: the optics (1) and the laser light sheet (2) of the PIV system; the chamber (4); the cooler (3) at the top surface and the heater (5) at the bottom surface; the data recorder (6) for temperature measurement system; the CCD camera (7) and the generator of incense smoke (8) for the PIV measurements.

through two inlets and flows out through two outlets located at the side wall of the cooling system.

We study the effects of complex terrain on the structure of the velocity and temperature fields in temperature stratified turbulence. In the laboratory experiments complex terrain is modelled by a wavy bottom surface of the chamber which is manufactured from aluminium. The wavy bottom surface has a sinusoidal modulation containing 7 periods with wavelength 8 cm and amplitude 1 cm. A sketch of the experimental set-up is shown in Figs. 1 and 2. The results of these experiments are compared to those obtained in experiments with a smooth plane bottom surface at the same temperature difference between the top and bottom plates.

The temperature field is measured with a temperature probe equipped with 12 E-thermocouples (with the diameter of 0.13 mm and the sensitivity of $\approx 65 \mu\text{V}/\text{K}$) attached to a rod with a diameter 4 mm. The spacing between thermocouples along the rod is 22 mm. Each thermocouple is inserted into a 1 mm diameter and 45 mm long case. A tip of a thermocouple protruded at the length of 15 mm out of the case. Thermocouples of type *E* are used for the temperature measurements in the core flow, while thermocouples of type *K* are used for temperature measurements at the heater and the cooler. All thermocouples are built by a manufacturer ("The temperature handbook", Omega Engineering inc., Stanford, 2011). Calibrations of all E-thermocouples in the temperature probe have been performed for three experiments

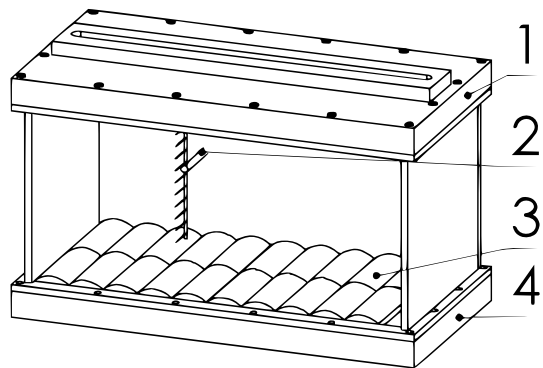


FIG. 2. A sketch of the chamber: the cooler (1) at the top surface; the heater (4) at the bottom surface; the temperature probe (2) equipped with 12 E-thermocouples; a wavy bottom surface (3) with a sinusoidal modulation.

with boiled water ($T = 373 \text{ K}$), the cold water with ice ($T = 273 \text{ K}$) and water with intermediate temperature ($T = 296 \text{ K}$). Comparisons have been performed using a precision temperature measurement manufactured device.

The temperature is measured for 11 rod positions with 20 mm intervals in the horizontal direction. This probe is used in the experiments with smooth plane bottom surface, while a temperature probe equipped with 13 E-thermocouples is used in the experiments with the wavy bottom surface. A sequence of 500 temperature readings for every thermocouple at every rod position is recorded and processed. We have measured the temperature field in many locations. Performing direct continuous measurements of the temperatures at the cooled top surface and at the heated bottom surface and using a standard device for supporting constant temperature difference ΔT between the top and bottom surfaces (Contact voltage regulator TDGC-2K), we control the constant temperature difference ΔT during the experiments.

The velocity field is measured using a Stereoscopic Particle Image Velocimetry. [54–56] In the experiments we use LaVision Flow Master III system. A double-pulsed light sheet is provided by a Nd-YAG laser (Continuum Surelite $2 \times 170 \text{ mJ}$). The light sheet optics includes spherical and cylindrical Galilei telescopes with tuneable divergence and adjustable focus length. We use the progressive-scan 12 bit digital CCD camera (with pixel size $6.7 \mu\text{m} \times 6.7 \mu\text{m}$ and 1280×1024 pixels) with a dual-frame-technique for cross-correlation processing of captured images. A programmable Timing Unit (PC interface card) generated sequences of pulses to control the laser, camera and data acquisition rate.

An incense smoke with sub-micron particles is used as a tracer for the PIV measurements. Smoke is produced by high temperature sublimation of solid incense grains. Analysis of smoke particles using a microscope (Nikon, Epiphot with an amplification of 560) and a PM-300 portable laser particulate analyzer shows that these particles have an approximately spherical shape and that

their mean diameter is of the order of $0.7\mu\text{m}$. The maximum tracer particle displacement in the experiment is of the order of $1/4$ of the interrogation window. The average displacement of tracer particles is of the order of 2.5 pixels. The average accuracy of the velocity measurements is of the order of 4% for the accuracy of the correlation peak detection in the interrogation window of the order of 0.1 pixel. [54–56]

We determine the mean and the r.m.s. velocities, two-point correlation functions and an integral scale of turbulence from the measured velocity fields. Series of 520 pairs of images acquired with a frequency of 2 Hz, are stored for calculating velocity maps and for ensemble and spatial averaging of turbulence characteristics. The center of the measurement region coincides with the center of the chamber. We measure velocity in a flow domain $256 \times 503 \text{ mm}^2$ with a spatial resolution of $393 \mu\text{m} / \text{pixel}$. The velocity field in the probed region is analyzed with interrogation windows of 32×32 pixels. In every interrogation window a velocity vector is determined from which velocity maps comprising 27×53 vectors are constructed. The mean and r.m.s. velocities for every point of a velocity map are calculated by averaging over 520 independent velocity maps, and the obtained averaged velocity map is averaged also over the central flow region.

The two-point correlation functions of the velocity field are determined for every point of the central part of the velocity map (with 16×16 vectors) by averaging over 520 independent velocity maps, which yields 16 correlation functions in horizontal and vertical directions. The two-point correlation function is obtained by averaging over the ensemble of these correlation functions. An integral scale of turbulence, ℓ , is determined from the two-point correlation functions of the velocity field. The turbulence time scale at the integral scale is $\tau = \ell / \sqrt{\langle \mathbf{u}^2 \rangle}$, where \mathbf{u} are the velocity fluctuations and $\sqrt{\langle \mathbf{u}^2 \rangle}$ is the r.m.s. of the velocity fluctuations. In the experiments we evaluated the variability between the first and the last 20 velocity maps of the series of the measured velocity field. Since very small variability is found, these tests show that 520 velocity maps contain enough data to obtain reliable statistical estimates. The size of the probed region does not affect our results.

In our study we employ a triple decomposition whereby the instantaneous temperature $T^{\text{tot}} = T + \theta$, where θ are the temperature fluctuations and T is the temperature determined by sliding averaging of the instantaneous temperature field over the time that is by one order of magnitude larger than the characteristic turbulence time. The temperature T is given by a sum, $T = \bar{T} + T^{\text{W}}$, where T^{W} are the long-term variations of the temperature T due to the large-scale standing internal gravity waves around the mean value \bar{T} . The mean temperature \bar{T} is obtained by the additional averaging of the temperature T over the time 400 s.

The time interval during which temperature field is measured at every point, is 400 s, which corresponds to 500 data points of the temperature field (over which

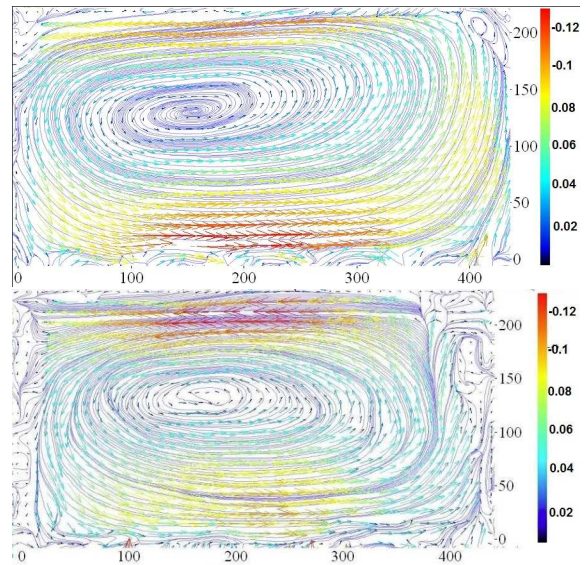


FIG. 3. The mean velocity patterns in the yz plane for the experiments with the wavy bottom surface (upper panel) and the smooth plane bottom surface (bottom panel) obtained at $\Delta T = 50 \text{ K}$. Here z and y are measured in mm and velocity is measured in m/s.

we perform averaging). In the temperature measurements, the acquisition frequency of the temperature is 1.25 Hz, and the corresponding acquisition time is 0.8 s. It is larger than the characteristic turbulence time (see below), and is much smaller than the period of the long-term oscillations of the mean temperature caused by internal gravity waves. Therefore, the acquisition frequency of temperature is high enough to provide sufficiently long time series for statistical estimation of the mean temperature \bar{T} and the long-term variations T^{W} of the temperature due to the large-scale internal gravity waves. Similar experimental set-ups, measurement techniques for temperature and velocity fields and data processing procedures have been used previously in our experimental study of different aspects of turbulent convection [57, 58] and stably stratified turbulence. [59, 60]

IV. EXPERIMENTAL RESULTS

In this section we describe experimental results related to formation of stably stratified regions in turbulent convection and excitation of internal gravity waves. We perform two sets of experiments with a wavy bottom surface and a smooth plane bottom surface for the same imposed mean temperature difference ΔT between the bottom and upper surfaces of the chamber. The velocity measurements show that in the both sets of experiments, a single large-scale circulation is observed for the temperature differences $\Delta T = 40 \text{ K}$ and $\Delta T = 50 \text{ K}$. In Fig. 3 we show the mean velocity patterns obtained in the experiments with the wavy bottom surface (upper panel)

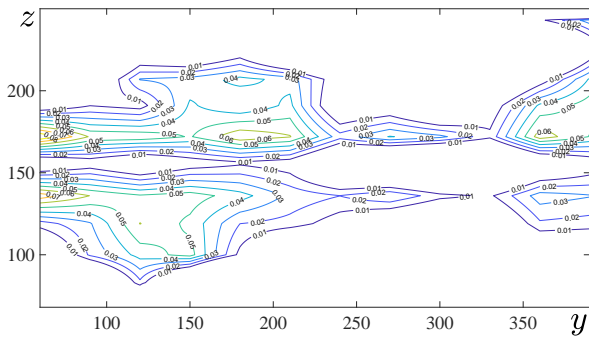


FIG. 4. Isolines in yz plane of the vertical mean temperature gradient $\nabla_z \overline{T}$ inside the large-scale circulation in the experiments with the wavy bottom surface for $\Delta T = 50$ K. Only the regions with positive vertical mean temperature gradient are shown. Here y and z are measured in mm, and the mean temperature gradient is measured in K/cm.

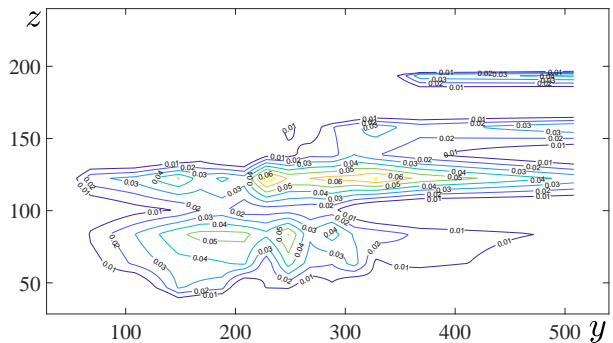


FIG. 6. Isolines in yz plane of the vertical mean temperature gradient $\nabla_z \overline{T}$ inside the large-scale circulation in the experiments with the wavy bottom surface for $\Delta T = 40$ K. Only the regions with positive vertical mean temperature gradient are shown. Here y and z are measured in mm, and the mean temperature gradient is measured in K/cm.

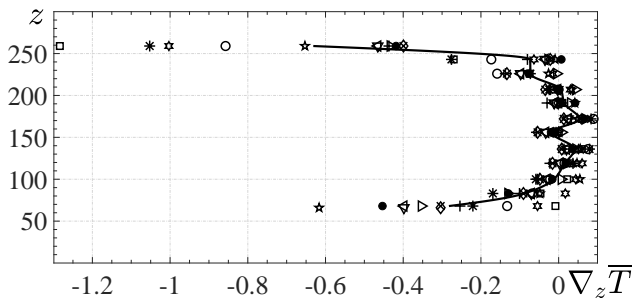


FIG. 5. Mean profile of the vertical mean temperature gradient $\nabla_z \overline{T}$ in the experiments with the wavy bottom surface for $\Delta T = 50$ K obtained by averaging over 15 vertical profiles measured in different cross-sections for different y inside the large-scale circulation. Here the height z is measured in mm, and the mean temperature gradient is measured in K/cm.

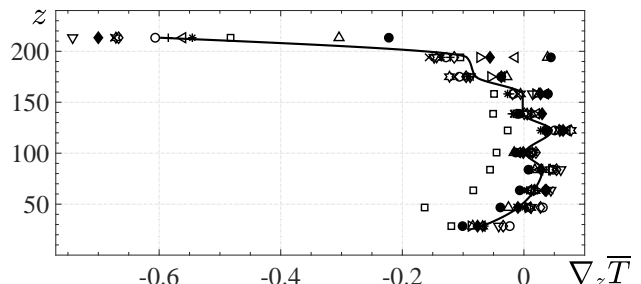


FIG. 7. Mean profile of the vertical mean temperature gradient $\nabla_z \overline{T}$ in the experiments with the wavy bottom surface for $\Delta T = 40$ K obtained by averaging over 15 vertical profiles measured in different cross-sections for different y inside the large-scale circulation. Here the height z is measured in mm, and the mean temperature gradient is measured in K/cm.

and smooth plane bottom surface (bottom panel). A difference in the mean velocity patterns is seen at the vicinity of the wavy bottom surface where the flows with the sinusoidal modulation of the mean velocity field are observed (see upper panel in Fig. 3). For lower and higher temperature differences between the bottom and top surfaces of the chamber, two large-scale circulations are observed and the mean temperature field is more complicated. This case will be investigated in a separate study. Experiments with smaller L_z increases aspect ratio of the chamber, where more than two large-scale circulations can be observed and the mean temperature field will be much more complicated. This case will be also investigated in a separate study.

Let us discuss parameters in the experiments. The characteristic turbulence time is $\tau = 0.28 - 0.62$ seconds, while the characteristic period for the large-scale circulatory flow is about 10 seconds, which is by order of magnitude larger than the turbulence time τ . These two characteristic times are much smaller than the time during which the velocity fields are measured (~ 260 seconds).

The maximum Rayleigh number, $Ra = \alpha g L_z^3 \Delta T / (\nu \kappa)$, in the turbulent convection is about 10^8 , where α is the thermal expansion coefficient, ν is the kinematic viscosity, κ is the thermal diffusivity, and L_z is the height measured from the lower point of a wavy surface with the sinusoidal modulation to the upper surface of the chamber.

The temperature measurements in the experiments with a wavy bottom surface show that the mean temperature gradient in the flow core inside the large-scale circulation is directed upward ($\nabla_z \overline{T} > 0$), that corresponds to a stably stratified flow. For instance, in Figs. 4 and 6 we plot isolines of the vertical mean temperature gradient $\nabla_z \overline{T}$ inside the large-scale circulation in yz plane where we show the regions with the positive vertical mean temperature gradient only. In Figs. 5 and 7 we also plot mean profiles of the vertical mean temperature gradient $\nabla_z \overline{T}$ obtained in these experiments by averaging over 15 vertical profiles measured in different cross-sections for different y inside the large-scale circulation. We discuss here the results of the experiments performed for two values of

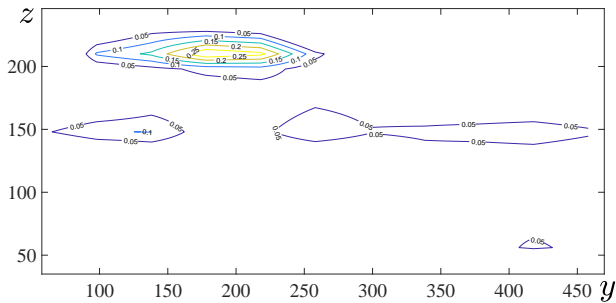


FIG. 8. Isolines in yz plane of the vertical mean temperature gradient $\nabla_z \bar{T}$ inside the large-scale circulation in the experiments with the smooth plane bottom surface for $\Delta T = 50$ K. Only the regions with positive vertical mean temperature gradient are shown. Here y and z are measured in mm, and the mean temperature gradient is measured in K/cm.

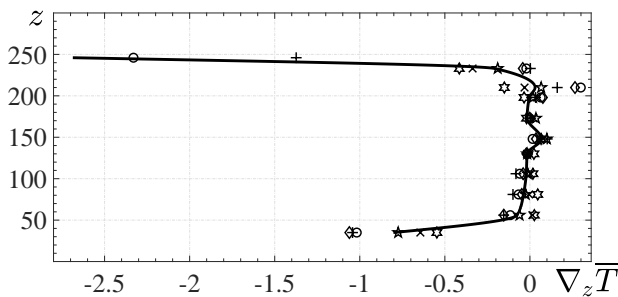


FIG. 9. Mean profile of the vertical mean temperature gradient $\nabla_z \bar{T}$ in the experiments with the smooth plane bottom surface for $\Delta T = 50$ K obtained by averaging over 11 vertical profiles measured in different cross-sections for different y inside the large-scale circulation. Here the height z is measured in mm, and the mean temperature gradient is measured in K/cm.

the temperature difference ΔT between the bottom and top surfaces: $\Delta T = 50$ K (Figs. 4 and 6) and $\Delta T = 40$ K (Figs. 5 and 7). All measurements have been done in the plane $x = 0.5L_x$. The accuracy of the mean temperature measurements is about 0.07 % (i.e. the accuracy is about 0.2 K for typical mean temperatures ≈ 300 K). The accuracy of the mean temperature gradient measurements is about 5 % for $\nabla_z \bar{T} \approx 0.1$ K/cm, and it is about 10 % for $\nabla_z \bar{T} \approx 0.01$ K/cm.

As can be seen in Fig. 4, there are two regions with positive mean temperature gradient separated by the region with negative mean temperature gradient in the center of the core flow. In the regions with negative vertical mean temperature gradient, the value of $N^2 \leq 0$ and the internal gravity waves cannot exist in these regions. This means that in the experiments with $\Delta T = 50$ K, there are two waveguides for the internal gravity waves. On the other hand, as can be seen in Fig. 6 ($\Delta T = 40$ K) there is one large region with positive mean temperature gradient which corresponds to a one waveguide. Similar trends can be seen in Figs. 5 and 7. In these experiments the

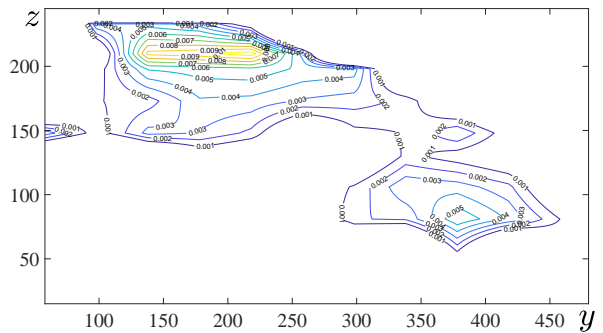


FIG. 10. Isolines in yz plane of the vertical mean temperature gradient $\nabla_z \bar{T}$ inside the large-scale circulation in the experiments with the smooth plane bottom surface for $\Delta T = 40$ K. Only the regions with positive vertical mean temperature gradient are shown. Here y and z are measured in mm, and the mean temperature gradient is measured in K/cm.

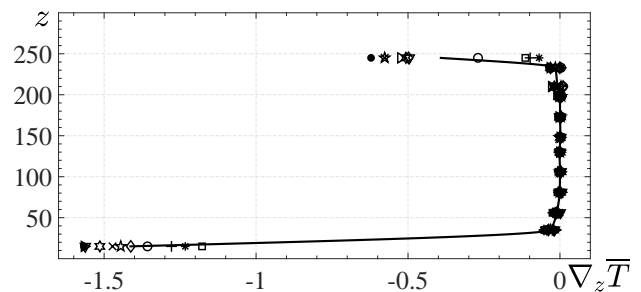


FIG. 11. Mean profile of the vertical mean temperature gradient $\nabla_z \bar{T}$ in the experiments with the smooth plane bottom surface for $\Delta T = 40$ K obtained by averaging over 11 vertical profiles measured in different cross-sections for different y inside the large-scale circulation. Here the height z is measured in mm, and the mean temperature gradient is measured in K/cm.

maximum gradient Richardson number, $Ri = N^2/Sh^2$, based on the mean velocity shear, Sh , of the large-scale circulation is about 1.

For comparison of results in two types of experiments with wavy and smooth plane bottom surfaces, in Figs. 8 and 10 we show isolines of the vertical mean temperature gradient $\nabla_z \bar{T}$ in yz plane inside the large-scale circulation obtained in the experiments with the smooth plane bottom surface. Similarly, in Figs. 9 and 11 we also show mean profiles of the vertical mean temperature gradient $\nabla_z \bar{T}$ obtained in these experiments by averaging over 11 vertical profiles measured in different cross-sections for different y inside the large-scale circulation. Here Figs. 8 and 9 correspond to the experiments with $\Delta T = 50$ K, while Figs. 10 and 11 are for the experiments with $\Delta T = 40$ K.

Figures 4–11 demonstrate that the spatial distributions of the vertical mean temperature gradient $\nabla_z \bar{T}$ in the experiments with the smooth plane bottom surface are essentially different from those obtained in the experiments with the wavy bottom surface. In particular,

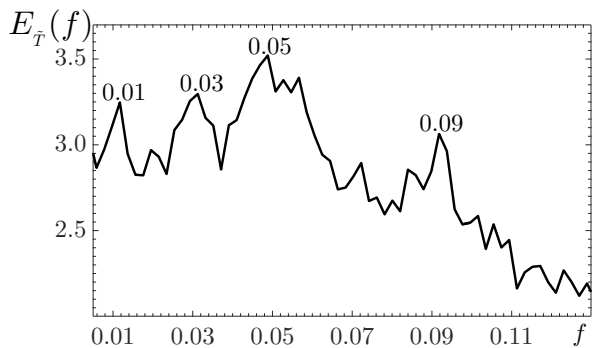


FIG. 12. The averaged spectrum function $E_{\tilde{T}}(f)$ of the temperature field obtained in the experiments for the temperature differences $\Delta T = 50$ K. The main frequencies of the large-scale internal gravity waves measured in Hz are indicated above the maxima of \tilde{T} . The function $\tilde{T}(f)$ is measured in K^2/Hz .

in the experiments with the smooth plane bottom surface, there are much less locations with positive vertical mean temperature gradient $\nabla_z \bar{T}$ than those in the experiments with the wavy bottom surface (compare Figs. 4 and 8 for $\Delta T = 50$ K). Also in the experiments with $\Delta T = 40$ K, the vertical mean temperature gradient $\nabla_z \bar{T}$ in the experiments with the smooth plane bottom surface are much smaller than those in the experiments with the wavy bottom surface.

These differences are one of the main reasons why we do not observe internal gravity waves in the experiments with the smooth plane bottom surface (see below). Another reason for the effective generation of internal gravity waves by the wavy bottom surface is the following. It is known in atmospheric physics that interaction of a strong wind with mountains is the key source of generation of internal gravity waves.[17, 18] Similar situation occurs during an interaction of the mean flow with the wavy bottom surface which produces the standing internal gravity waves in our experiments.

To study internal gravity waves, we determine spectrum of the long-term variations of the temperature field characterising the large-scale waves. From this spectral analysis we obtain main frequencies of internal gravity waves. The spectrum function $E_T(f) = \tilde{T}(f)T^*(f)$ for the temperature field (containing 250 frequency data points) has been determined at 80 locations of the stably stratified region, where the temperature $\tilde{T}(t) = T^{\text{tot}} - \bar{T}$ and $\tilde{T}(f)$ is its Fourier component. For every frequency f , the obtained spectrum functions $E_T(f)$ have been averaged over 80 locations. In Figs. 12 and 13 we show the volume averaged spectrum function $E_{\tilde{T}}(f) = \langle E_T(f) \rangle_{\text{vol}}$ of the temperature field in the experiments for the temperature differences $\Delta T = 50$ K and $\Delta T = 40$ K, respectively, where the brackets $\langle \dots \rangle_{\text{vol}}$ denote the averaging over 80 locations.

Comparing the main frequencies of internal gravity

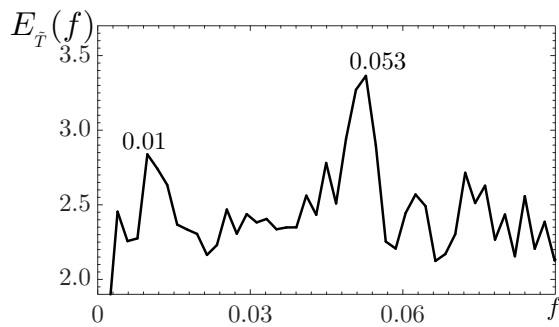


FIG. 13. The averaged spectrum function $E_{\tilde{T}}(f)$ of the temperature field obtained in the experiments for the temperature differences $\Delta T = 40$ K. The main frequencies of the large-scale internal gravity waves measured in Hz are indicated above the maxima of \tilde{T} . The function $\tilde{T}(f)$ is measured in K^2/Hz .

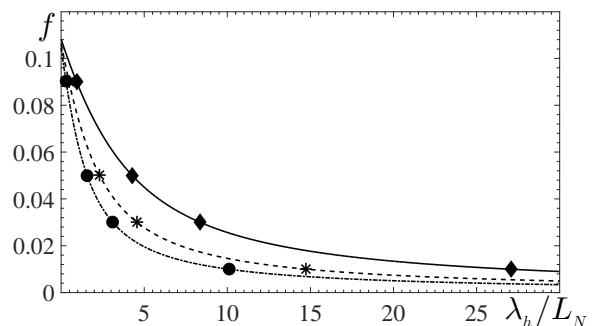


FIG. 14. The frequencies of the internal gravity waves (measured in Hz) versus the normalized horizontal wavelength λ_h/L_N : theoretical curves for different modes $m = 1$ (solid), $m = 2$ (dashed) and $m = 3$ (dashed-dotted) and measured frequencies associated with different modes: $m = 1$ (diamonds), $m = 2$ (snowflakes) and $m = 3$ (circles) in the experiments for $\Delta T = 50$ K.

waves obtained in the temperature measurements with the profile of the Brunt-Väsälä frequency (based on the measured profile of the mean temperature gradient), we determine the horizontal wave-numbers for the observed internal gravity waves. Figures 14 and 15 show the theoretical dependencies for the frequencies of the internal gravity waves versus the normalized horizontal wavelength λ_h/L_N given by Eq. (17), where L_N is the characteristic vertical scale of the Brunt-Väsälä frequency variations and $\lambda_h = 2\pi/k_h$ is the horizontal wavelength. The theoretical curves are plotted for the first three main modes of the large-scale internal gravity waves.

Using the theoretical curves and the measured frequencies of the long-term variations of the temperature fields in the experiments with the temperature differences $\Delta T = 50$ K (Fig. 14) and $\Delta T = 40$ K (Fig. 15), we determine the horizontal wavelenghtes associated with different modes of the large-scale internal gravity waves. In the experiments with $\Delta T = 40$ K where there is only

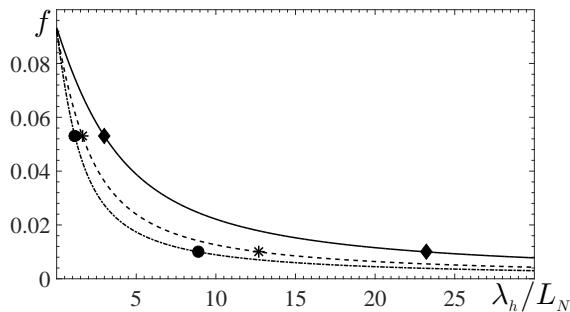


FIG. 15. The frequencies of the internal gravity waves (measured in Hz) versus the normalized horizontal wavelength λ_h/L_N : theoretical curves for different modes $m = 1$ (solid), $m = 2$ (dashed) and $m = 3$ (dashed-dotted) and measured frequencies associated with different modes: $m = 1$ (diamonds), $m = 2$ (snowflakes) and $m = 3$ (circles) in the experiments for $\Delta T = 40$ K.

a one waveguide (see Figs. 6) for the large-scale internal gravity waves, we observe two dominant modes (see Fig. 15), while in the experiments with $\Delta T = 50$ K where there are two waveguides (see Figs. 4), we observe four main wave frequencies (two in the each waveguide), see Fig. 14. Note that inside the chamber, we observe standing but not propagating internal gravity waves because the chamber is a small closed volume. Actually, interactions of propagating and reflecting waves cause the standing internal gravity waves, which are observed in the experiments with the wavy bottom surface.

To compare the results on velocity fluctuations measured in the two sets of experiments with the wavy and smooth plane bottom surfaces, conducted at the same mean temperature difference between bottom and upper surfaces, we show in Fig. 16 the vertical profiles of the rms velocity components $u_y^{\text{rms}} = \sqrt{\langle u_y^2 \rangle}$ and $u_z^{\text{rms}} = \sqrt{\langle u_z^2 \rangle}$. In the experiments with the wavy bottom surface, there is a minimum in the vertical profile of the rms velocities in the center part of the chamber. On the other hand, in the experiments with the smooth plane bottom surface, the vertical distribution of the rms velocities is essentially less inhomogeneous. Also the values of turbulent velocities in the experiments with the wavy bottom surface are smaller compared to velocity fluctuations in the experiments with the smooth plane bottom surface.

The reason for these differences may be as follows. In the experiments with the wavy bottom surface, the intensity of the velocity fluctuations are partially depleted by the production of the temperature fluctuations in stably stratified regions, where the part of turbulent kinetic energy is transformed to the turbulent potential energy caused by the temperature fluctuations. In another words, in stably stratified flows, the production of turbulent kinetic energy is depleted by destruction caused by the buoyancy. [34, 37] On the other hand, in the experiments with the smooth plane bottom surface, there are much less locations of the stably stratified regions,

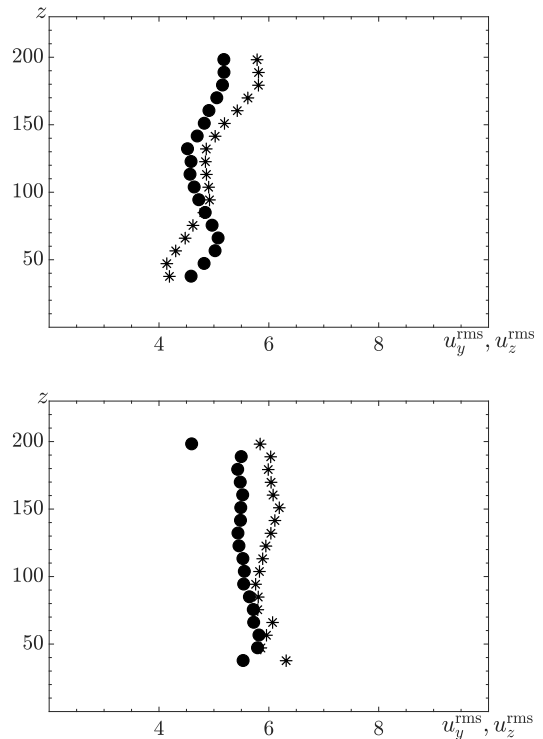


FIG. 16. The vertical profiles of the rms velocities u_y^{rms} (snowflakes) and u_z^{rms} (circles) in the experiments with the wavy bottom surface (upper panel) and the smooth plane bottom surface (bottom panel) obtained at $\Delta T = 50$ K. Here the z is measured in mm, and the rms velocities u_y^{rms} and u_z^{rms} are measured in cm/s.

and the level of velocity fluctuations is larger in comparison with that observed in the experiments with the wavy bottom surface.

V. CONCLUSIONS

In the present study we perform laboratory experiments in convection over a wavy heated bottom surface. An interaction of the large-scale circulation with the wavy heated bottom surface strongly affects the spatial structure of the mean temperature field and generation of the large-scale standing internal gravity waves in the flow core. In particular, we have found that there are many locations with stably stratified regions in the flow core of the large-scale circulation, and the large-scale standing internal gravity waves are observed in these regions. The spectrum of these waves contains several localized maxima, that is an indication of existence of the waveguide resonators for the internal gravity waves. On the other hand, in the experiments with a smooth plane bottom surface at the same temperature difference between bottom and upper surfaces, there are less locations with a stably stratified turbulence and the internal grav-

ity waves are not detected there. The turbulence in the region with stably stratified flows in the experiments with the wavy bottom surface is inhomogeneous, e.g., there is a minimum in the vertical profiles of the rms velocities in the center part of the chamber, where the intensity of the velocity fluctuations are partially depleted by the production of the temperature fluctuations. On the other hand, in the experiments with the smooth plane bottom surface, the vertical distribution of the rms velocities is nearly homogeneous.

ACKNOWLEDGMENTS

We thank A. Krein for his assistance in construction of the experimental set-up. This research was supported in part by the Israel Science Foundation governed by the Israel Academy of Sciences (grant No. 1210/15) and by Ministry of Science and Technology (grant No. 3-16516).

Appendix A: Nomenclature

c_p is the specific heat at constant pressure,
 c_v is the specific heat at constant volume,
 e is the vertical unit vector,
 $E_T(f)$ is the spectrum function for the temperature field,
 $E_{\bar{T}}(f)$ is the volume averaged spectrum function for the temperature field,
 f is the frequency,
 g is the acceleration due to gravity,
 k is the wave vector,
 $k_h = (k_x, k_y)$ is the horizontal component of the wave vector,
 k_z is the vertical component of the wave vector,
 ℓ is the integral scale of turbulence,
 L_N is the characteristic scale of the Brunt-Väisälä frequency variations,
 L_x and L_y are the horizontal sizes of the chamber along the x and y axes,
 L_z is the height measured from the lower point of a wavy surface with the sinusoidal modulation to the upper surface of the chamber,

$N(z) = (g\nabla_z S_{\text{eq}})^{1/2}$ is Brunt-Väisälä frequency,
 P_{eq} is the pressure at an equilibrium,
 P^W are the pressure perturbations,
 r is the radius-vector of the centre of the wave packet,
 Ra is the Rayleigh number,
 Ri is the gradient Richardson number,
 S_{eq} is the entropy at an equilibrium,
 S^W are the entropy perturbations,
 Sh is the mean velocity shear of the large-scale circulation,
 T^{tot} is the total instantaneous temperature,
 T is the temperature determined by sliding averaging of the instantaneous total temperature field,
 \bar{T} is the mean temperature,
 T_{eq} is the temperature at an equilibrium,
 T^W are the temperature perturbations (the long-term variations of the temperature due to the large-scale standing internal gravity waves),
 $\tilde{T}(f)$ is the Fourier component of the temperature deviation $\tilde{T}(t) = T^{\text{tot}} - \bar{T}$,
 ΔT is the temperature difference between the bottom and upper surfaces of the chamber,
 V_* is the amplitude of the vertical velocity for the wave field,
 $V_{\text{eq}}0$ is the velocity at an equilibrium,
 V^W are the velocity perturbations (the long-term variations of the velocity due to the large-scale standing internal gravity waves),
 $V_{\perp}^W = (V_x^W, V_y^W)$ is the horizontal component of the velocity perturbations,
 u are the velocity fluctuations,
 u_y^{rms} is the rms of the turbulent horizontal velocity,
 u_z^{rms} is the rms of the turbulent vertical velocity,
 z_{max} is the reflection (or "turning") point,
 α is the thermal expansion coefficient,
 $\gamma = c_p/c_v$ is the ratio of the specific heats,
 θ are the temperature fluctuations,
 κ is the thermal diffusivity,
 λ_h is the horizontal wavelength,
 ν is the kinematic viscosity,
 ρ_{eq} is the density at an equilibrium,
 τ is the turbulence time scale at the integral scale of turbulence,
 φ is the phase of the velocity perturbations,
 ω is the frequency of the internal gravity waves.

-
- [1] J. S. Turner, *Buoyancy Effects in Fluids* (Cambridge University Press, Cambridge, 1973).
[2] A. S. Monin and A. M. Yaglom, *Statistical Fluid Mechanics* (MIT Press, Cambridge, Massachusetts, 1975), Vol. 2.
[3] J. C. Kaimal and J. J. Fennigan, *Atmospheric Boundary Layer Flows* (Oxford University Press, New York, 1994).
[4] S. S. Zilitinkevich, *Turbulent Penetrative Convection* (Avebury Technical, Aldershot, 1991).
[5] J. R. Garratt, *The Atmospheric Boundary Layer* (Cambridge University Press, Cambridge 1992).
[6] S. V. Nazarenko, *Wave Turbulence*, Lecture Notes in Physics, vol. 825 (Springer, Heidelberg, 2011).
[7] E. S. C. Ching, *Statistics and Scaling in Turbulent Rayleigh-Bnard Convection* (Springer, Singapore, 2014).
[8] G. Ahlers, S. Grossmann, D. Lohse, "Heat transfer and large scale dynamics in turbulent Rayleigh-Bnard convection," *Rev. Mod. Phys.* **81**, 503-537 (2009).
[9] D. Lohse, K.-Q. Xia, "Small-scale properties of turbulent Rayleigh-Bnard convection," *Annu. Rev. Fluid Mech.* **42**,

- 335-363 (2010).
- [10] F. Chillà, J. Schumacher, "New perspectives in turbulent Rayleigh-Bénard convection," *Eur. Phys. J. E* **35**, 58 (2012).
- [11] T. Beer, *Atmospheric Waves* (Wiley, New York, 1974).
- [12] E. E. Gossard and W. H. Hooke, *Waves in the Atmosphere* (Elsevier, New York, 1975).
- [13] Yu. Z. Miropol'sky, *Dynamics of Internal Gravity Waves in the Ocean* (Springer, Dordrecht, 2001).
- [14] C. J. Nappo, *An Introduction to Atmospheric Gravity Waves*, (Academic Press, London, 2002).
- [15] B. R. Sutherland, *Internal Gravity Waves* (Cambridge Univ. Press, Cambridge, 2010).
- [16] C. Garrett and W. Munk, "Internal waves in the ocean," *Annu. Rev. Fluid Mech.* **11**, 339-369 (1979).
- [17] D. C. Fritts and M. J. Alexander, "Gravity wave dynamics and effects in the middle atmosphere," *Rev. Geophys.* **41**, 1003, 1-64 (2003).
- [18] C. Staquet and J. Sommeria, "Internal gravity waves: From instabilities to turbulence," *Annu. Rev. Fluid Mech.* **34**, 559-593 (2002).
- [19] J. J. Finnigan and F. Einaudi, "The interaction between an internal gravity wave and the planetary boundary layer. Part II: Effect of the wave on the turbulence structure," *Quart. J. Roy. Met. Soc.* **107**, 807-832 (1981).
- [20] J. J. Finnigan, F. Einaudi and D. Fua, "The interaction between an internal gravity wave and turbulence in the stably-stratified nocturnal boundary layer," *J. Atmosph. Sci.* **41**, 2409-2436 (1984).
- [21] F. Einaudi, J. J. Finnigan and D. Fua, "Gravity wave turbulence interaction in the presence of a critical level," *J. Atmosph. Sci.* **41**, 661-667 (1984).
- [22] J. J. Finnigan, "Kinetic energy transfer between internal gravity waves and turbulence," *J. Atmosph. Sci.* **45**, 486-505 (1988).
- [23] J. J. Finnigan, "A note on wave-turbulence interaction and the possibility of scaling the very stable boundary layer," *Boundary-Layer Meteorol.* **90**, 529-539 (1999).
- [24] F. Einaudi and J. J. Finnigan, "Wave-turbulence dynamics in the stably stratified boundary layer," *Atmosph. Sci.* **50**, 1841-1864 (1993).
- [25] G. Chimonaas, "Steps, waves and turbulence in the stably stratified planetary boundary layer," *Boundary-Layer Meteorol.* **90**, 397-421 (1999).
- [26] S. S. Zilitinkevich, "Third-order transport due to internal waves and non-local turbulence in the stably stratified surface layer," *Quart. J. Roy. Met. Soc.* **128**, 913-925 (2002).
- [27] L. H. Jin, R. M. C. So and T. B. Gatski, "Equilibrium states of turbulent homogeneous buoyant flows," *J. Fluid Mech.* **482**, 207-233 (2003).
- [28] H. Baumert and H. Peters, "Turbulence closure, steady state, and collapse into waves," *J. Phys. Oceanogr.* **34**, 505-512 (2004).
- [29] H. Baumert and H. Peters, "Turbulence closure: turbulence, waves and the wave-turbulence transition Part I: Vanishing mean shear," *Ocean Sci.* **5**, 47-58 (2009).
- [30] F. G. Jacobitz, M. M. Rogers and J. H. Ferziger, "Waves in stably stratified turbulent flow," *J. Turbulence* **6**, 1-12 (2005).
- [31] J. Sun, C. J. Nappo, L. Mahrt, D. Belusíc, B. Grisogono, et al., "Review of wave-turbulence interactions in the stable atmospheric boundary layer," *Rev. Geophys.* **53**, 956-993 (2015).
- [32] S. S. Zilitinkevich, T. Elperin, N. Kleeorin, V. L'vov and I. Rogachevskii, "Energy- and flux-budget (EFB) turbulence closure model for stably stratified flows. Part II: The role of internal gravity waves," *Boundary-Layer Meteorol.* **133**, 139-164 (2009).
- [33] N. Kleeorin, I. Rogachevskii, I. A. Soustova, Yu. I. Troitskaya, O. S. Ermakova, S. S. Zilitinkevich, "Internal gravity waves in the energy and flux budget turbulence-closure theory for shear-free stably stratified flows," *Phys. Rev. E* **99**, 063106 (2019).
- [34] S. S. Zilitinkevich, T. Elperin, N. Kleeorin and I. Rogachevskii, "Energy- and flux-budget (EFB) turbulence closure model for the stably stratified flows. Part I: Steady-state, homogeneous regimes," *Boundary-Layer Meteorol.* **125**, 167-192 (2007).
- [35] S. S. Zilitinkevich, T. Elperin, N. Kleeorin, I. Rogachevskii, I. Esau, T. Mauritsen and M. Miles, "Turbulence energetics in stably stratified geophysical flows: strong and weak mixing regimes," *Quart. J. Roy. Meteorol. Soc.* **134**, 793-799 (2008).
- [36] S. S. Zilitinkevich, I. Esau, N. Kleeorin, I. Rogachevskii and R. D. Kouznetsov, "On the velocity gradient in the stably stratified sheared flows. Part I: Asymptotic analysis and applications," *Boundary-Layer Meteorol.* **135**, 505-511 (2010).
- [37] S. S. Zilitinkevich, T. Elperin, N. Kleeorin, I. Rogachevskii, and I. Esau, "A hierarchy of energy- and flux-budget (EFB) turbulence closure models for stably stratified geophysical flows," *Boundary-Layer Meteorol.* **146**, 341-373 (2013).
- [38] S. Toppaladoddi, S. Succi, and J. S. Wettlaufer, "Roughness as a route to the ultimate regime of thermal convection," *Phys. Rev. Lett.* **118**, 074503 (2017).
- [39] J. J. Niemela, L. Skrbek, K. R. Sreenivasan and R. J. Donnelly, "The wind in confined thermal convection," *J. Fluid Mech.* **449**, 169 (2001).
- [40] P. G. Baines, *Topographic effects in stratified flows* (Cambridge University Press, New York, 1995).
- [41] R. E. Kelly, D. Pal, "Thermal convection with spatially periodic boundary conditions: resonant wavelength excitation," *J. Fluid Mech.* **86**, 433-456 (1978).
- [42] G. Seiden, S. Weiss, J. McCoy, W. Pessch, E. Bodenschatz, "Pattern forming system in the presence of different symmetry-breaking mechanisms," *Phys. Rev. Lett.* **101**, 214503 (2008).
- [43] S. Weiss, G. Seiden, E. Bodenschatz, "Pattern formation in spatially forced thermal convection," *New J. Phys.* **14**, 053010 (2012).
- [44] S. Weiss, G. Seiden, E. Bodenschatz, "Resonance patterns in spatially forced Rayleigh-Bénard convection," *J. Fluid Mech.* **756**, 293-308 (2014).
- [45] G. Freund, W. Pesch, W. Zimmermann, "Rayleigh-Bénard convection in the presence of spatial temperature modulations," *J. Fluid Mech.* **673**, 318-348 (2011).
- [46] X. Zhu, R. J. A. M. Stevens, R. Verzicco, D. Lohse, "Roughness-facilitated local 1/2 scaling does not imply the onset of the ultimate regime of thermal convection," *Phys. Rev. Lett.* **119**, 154501 (2017).
- [47] P.-E. Roche, B. Castaing, B. Chabaud, and B. Hébral, "Observation of the 1/2 power law in Rayleigh-Bénard convection," *Phys. Rev. E* **63**, 045303 (2001).
- [48] G. Stringano, G. Pascazio, and R. Verzicco, "Turbulent thermal convection over grooved plates," *J. Fluid Mech.* **557**, 307-336 (2006).

- [49] R. H. Kraichnan, "Turbulent thermal convection at arbitrary Prandtl number," *Phys. Fluids* **5**, 1374-1389 (1962).
- [50] S. Grossmann and D. Lohse, "Multiple scaling in the ultimate regime of thermal convection," *Phys. Fluids* **23**, 045108 (2011).
- [51] S. Weinberg, "Eikonal method in magnetohydrodynamics," *Phys. Rev.* **126**, 1899-1909 (1962).
- [52] L. D. Landau and E. M. Lifshitz, *Quantum Mechanics: Non-Relativistic Theory*, Vol. **3** (Elsevier, Chicago, 2013).
- [53] A. S. Davidov, *Quantum Mechanics* (Pergamon Press, N.Y., 1965).
- [54] R. J. Adrian, "Particle-imaging techniques for experimental fluid mechanics," *Annu. Rev. Fluid Mech.* **23**, 261 (1991).
- [55] M. Raffel, C. Willert, S. Werely and J. Kompenhans, *Particle Image Velocimetry* (Springer, Berlin-Heidelberg, 2007).
- [56] J. Westerweel, "Theoretical analysis of the measurement precision in particle image velocimetry," *Experim. Fluids* **29**, S3 (2000).
- [57] A. Eidelman, T. Elperin, N. Kleeorin, A. Markovich and I. Rogachevskii, "Hysteresis phenomenon in turbulent convection," *Experim. Fluids* **40**, 723-732 (2006).
- [58] M. Bukai, A. Eidelman, T. Elperin, N. Kleeorin, I. Rogachevskii and I. Sapir-Katiraie, "Effect of large-scale coherent structures on turbulent convection," *Phys. Rev. E* **79**, 066302 (2009).
- [59] M. Bukai, A. Eidelman, T. Elperin, N. Kleeorin, I. Rogachevskii and I. Sapir-Katiraie, "Transition phenomena in unstably stratified turbulent flows," *Phys. Rev. E* **83**, 036302 (2011).
- [60] A. Eidelman, T. Elperin, I. Gluzman, N. Kleeorin and I. Rogachevskii, "Experimental study of temperature fluctuations in forced stably stratified turbulent flows," *Phys. Fluids* **25**, 015111 (2013).